On Interacting Damage Mechanisms in Laminated Composites subjected to High Amplitude Fatigue

Michael J. Bogdanor[a], Stephen B. Clay[b] and Caglar Oskay[a*]

[a]Department of Civil and Environmental Engineering
Vanderbilt University, Nashville, TN 37235, USA

[b]Aerospace Systems Directorate
Air Force Research Laboratory, WPAFB, OH 45433, USA

Abstract

This manuscript provides a combined computational-experimental investigation of the interaction of damage mechanisms in carbon fiber reinforced polymer (CFRP) laminated composites subjected to fatigue loading. The investigations particularly focus on [60,0,-60]$_{3S}$ laminates, whose behavior demonstrates strong interactions between the relevant damage modes. Numerical investigations are performed using a spatio-temporal computational homogenization-based multiscale life prediction model. The computational approach relies on a model order reduction methodology to develop a meso-model that can capture the relevant failure mechanisms in a computationally efficient manner. The model was calibrated using a suite of experimental data from the static and fatigue response of simple laminates made of the same constituents. The calibrated model along with experimental observations from acoustic emission and X-ray computed tomography were employed to understand the relative roles of delamination and splitting, and their interactions in controlling fatigue failure processes in CFRPs.

Keywords: Polymer-matrix composites; Fatigue; Computational modelling; Damage mechanics.

*Corresponding Author: VU Station B#351831, 2301 Vanderbilt Place, Nashville, TN 37235. Email: caglar.oskay@vanderbilt.edu

1 Introduction

The state of damage in laminated composite structures subjected to fatigue loading has a significant effect on the remaining life and the residual strength. Early works on fatigue modeling focused on identification of *damage markers* or characteristic states of damage that correlate well with the prediction metrics such as life, residual strength or residual stiffness (e.g., [25]). While this approach provides accurate predictions for some laminate layups and geometries, damage markers may significantly differ from one laminate configuration to another, and therefore the approach does not generalize to arbitrary laminate configurations. The difficulty is largely due to the interactions between various damage mechanisms that depend on the constitutive and failure properties of the composite constituents, laminate stacking, ply thicknesses, loading profile, and structural geometry. In the context of carbon fiber reinforced polymers (CFRPs) subjected to tension-tension fatigue, understanding and modeling of the interactions between the transverse matrix cracks, longitudinal splits, fiber fracture and delaminations are critical to achieving reliable predictive capability when subjected to cyclic loading.

Damage mechanisms and their evolution under fatigue loading conditions of notched and unnotched specimens have been traditionally investigated separately. While the damage mechanisms in both types of specimens are typically the same, damage in unnotched specimens originates at edge singularities, whereas stress concentrations at the notch tip initiates damage in notched specimens. Mohandesi and Majidi [17] investigated the fatigue damage mechanisms of quasi-isotropic unnotched specimens. Off-axis matrix cracking and delamination between 90 degree and 45 degree plies at the exterior edges of the specimens constituted the initial damage. The propagation of delamination was relatively quick. Chen et al. [7] studied unnotched $[\pm 45,0_2]_{2S}$ specimens subjected to tension fatigue. Matrix cracking and fiber breaks preceded delamination damage with more delamination between ± 45 plies compared to 0-45 interfaces. Typical triangular delaminations observed in the specimens were a consequence of interacting transverse matrix cracks, which saturated and reached the characteristic damage state [22]. Gamstedt and Ostlund [12] and Gamstedt and Talreja [13] pointed to the interaction between local fiber breaks that induce the transverse matrix cracking, which consequently propagates through the fiber bridging mechanism in unidirectional specimens. Under relatively low load amplitudes, Gamstedt and coworkers indicated that the transverse matrix cracks are arrested by fiber-matrix debonding.

Spearing and Beaumont [24] investigated carbon-epoxy quasi-isotropic and cross ply specimens with elliptical notches subjected to tension fatigue. The primary damage mechanisms of longitudinal splitting in 0 degree plies, transverse matrix cracks and delaminations with size related to the length of the longitudinal splits were observed. Close examination of 0 degree plies around the notch tip revealed broken fibers particularly at the intersection of a split and the matrix cracks. This study found that the split length increased with additional fatigue cycles and that the longer split length was correlated with higher residual strength of the coupon. Afaghi-Katibi et al. [1] investigated the failure mechanisms in open-hole 0 degree unidirectional and cross ply laminates by controlling the fiber-matrix interfacial debonding properties through functionalization. Under high amplitude fatigue, they observed insignificant difference in fatigue life between laminates with strong and weak interfaces, confirming that fiber fracture propagation is the determining mechanism for fatigue life. Those laminates with weaker interfaces displayed *higher* residual strength pointing to a transition in load carrying mechanism as a function of interfacial properties, which also control interlaminar degradation. Ambu et al. [2] and Aymerich and Found [3] investigated the interacting damage mechanisms in notched and unnotched quasi-isotropic and cross-ply laminates. The failure sequence in both laminate types were matrix cracking and splitting followed by delaminations. Use of a thermoplastic matrix eliminated the longitudinal splitting in quasi-isotropic laminates, which led to early failure induced by fiber fracture propagation. In many of these investigations, thicker plies demonstrated a more gradual and widespread damage accumulation prior to failure. More recently, Nixon-Pearson et al. [18] performed a detailed damage investigation of a quasi-isotropic laminate. Under low amplitude loading, matrix damage within the surface plies and a small amount of splits without significant delamination were observed. The sequence of damage accumulation was longitudinal splitting and matrix cracking followed by triangular delaminations between 90 and 45 degree layers, and longitudinal delamination following splits between 45 and 0 degree layers. The propagation of longitudinal delamination and growth of splits were found to occur simultaneously and no conclusions could be drawn as to the sequencing between these two dominant damage modes.

The above-mentioned experimental investigations point to strong coupling between the propagation of damage modes, which significantly affect fatigue life and post-fatigue strength of composites. In this study, a combined computational-experimental investigation is performed to better understand the interaction effects of matrix cracking, splitting, delamination and fiber fracture under the fatigue loading. The investigations focus on $[60,0,-60]_{3S}$ laminates, whose behavior clearly demonstrate strong interactions between these damage modes. The numerical investigations are performed using a computational homogenization-based multiple spatio-temporal scale life prediction model [9, 10, 6]. The method is based on the mathematical homogenization theory [4, 26] applied to multiple length scales to capture material heterogeneity of the composite structure, and multiple time scales to address the tremendous disparity between a cycle of loading and the overall fatigue life of the composite. The computational model relies on the eigendeformation-based model order reduction methodology to devise a meso-model that can capture the relevant failure mechanisms in a computationally efficient manner [8, 19, 5, 23]. The computational model was calibrated using a suite of experimental data from static and fatigue response of simple laminates made of the same constituents. The calibrated model along with acoustic emission and X-ray computed tomography were employed to understand the relative roles of delamination and splitting. A parametric study explains the criticality of each damage mechanism in controlling the fatigue failure process.

The remainder of this manuscript is organized as follows: Section 2 details the experiments and the nondestructive testing procedures employed in this study. Section 3 summarizes the multiscale modeling approach employed to capture the progressive failure in the composites under fatigue. Section 4 outlines the parameter calibration and the description of the numerical specimen used in the investigations. Section 5 provides the results of the combined experimental-computational study. The effects of failure mode interactions are discussed in Section 6. The conclusions of this study are provided in Section 7.

2 Experiments

A series of monotonic and fatigue calibration experiments were conducted on IM7/977-3 graphite epoxy coupons that were hand laid and autoclave cured at a temperature of 177°C and a pressure of 689 kPa. Notched coupons with $[60,0,-60]_{3S}$ and $[+45,0,-45,90]_{2S}$ layups were fabricated, tested, and inspected. Five replicate specimens were cut from the panels for testing. Acid digestion testing was used to measure an average fiber volume fraction of the specimens of 64.2%. The average cured ply thickness was 0.128 mm.

The ASTM standard test methods (Table 1) were followed for each test. All experiments with the exception of the $[+45,0,-45,90]_{2S}$ and $[+60,0,-60]_{3S}$ layups were employed in the model calibration. All static tests were conducted under constant displacement rate loading. The rate for tension and shear tests was 2 mm/min, for compression tests was 1.5 mm/min, and for end notch flexure tests was 0.5 mm/min. All fatigue tests were performed using an R-ratio of 0.1 and a frequency of 10Hz.

A 25 mm gage length clip-on extensometer was used to measure the strain in the vicinity of the hole for notched specimens. Five replicates were loaded in monotonic tension to 90% of the ultimate stress, unloaded, and inspected using x-ray. After inspection, the monotonic tension specimens were loaded to failure. Five additional specimens were loaded in tension-tension fatigue to 80% ultimate stress for 2,000,000 cycles. These fatigue specimens were removed from the testing machine at 50,000 cycle increments for x-ray inspections.

Table 1: Experimental program.

	ASTM standard	Test configuration	Dimensions [mm^3]	Tab length [mm]	Tab bevel [degrees]	Hole diam. [mm]
static	D3039	$[0]_8$ tension	250x12.5x1	56	7	
	D3410	$[0]_{16}$ compression	140x12.5x2	63.5	90	
	D3410	$[90]_{24}$ compression	140x25.4x3	63.5	90	
	D790	$[90]_{16}$ 3pt bend	110x12.7x2			
	D3518	$[+45,-45]_{4S}$ tension	250x25.4x2			
	D7078	$[0/90]_{4S}$ v-notch shear	76x56x2			
	D7905	$[0]_{24}$ end notch flexure	250x25.4x3			
fatigue	D3479	$[0]_8$ tension-tension	250x12.7x1	56	7	
	D790	$[90]_{16}$ 3pt bend	60x12.7x2			
	D7905	$[0]_{24}$ end notch flexure	250x25.4x3			
	D3479	$[60,0,-60]_{3S}$ notched	250x38.1x2.3	56	7	6.35
	D3479	$[45,0,-45,90]_{2S}$ notched	250x38.1x2	56	7	6.35

2.1 Nondestructive Testing

In order to monitor damage accumulation during testing, a Micro-II Digital Acoustic Emission (AE) System was used to passively record the acoustic energy emitted from the composite material as matrix, fiber, and interfacial damage occurred. Prior to calibration testing, trial runs were performed on the AE system to define the appropriate signal conditioning parameters. An amplitude threshold of 53 dB was found to allow the detection of valid material failure events without recording ambient laboratory noise. A "hit" was registered when the acoustic energy detected by the sensors exceeded the predetermined amplitude threshold. The AE timing parameters used for this study were a peak definition time of 400 μs, a hit definition time of 800 μs, a hit lockout time of 200 μs, and a maximum duration of 100 ms, as recommended by the equipment manufacturer.

Standard X-ray radiography was used to characterize the damage of the notched test specimens. The specimens were inspected with a Philips X-ray system using a 160 kV source and 0.4 mm focal spot. A 50 μm sampling was used with IPS imaging plates and a General Electric CR Tower. Imaging parameters of 26 kV, 3 mA, and 30 s were used with a distance of 1,220 mm between the source and the detector. In order to improve the contrast between the damaged and undamaged regions of the composite, an opaque penetrant (Zinc Iodide) was applied to the edges of the specimens and absorbed into the open voids that were connected to the free edge of the specimen. The General Electric Rhythm image processing software was used to obtain the images of the damage. A Level III contrast enhancement filter was applied to each image using noise reduction and latitude correction.

X-Tek HMX160 X-Ray computed tomography (CT) system was used to characterize the damage in the specimens. The CT system consists of an X-ray source with a voltage of 90 kV and a current of 90 μA, a stage that rotates 360° at 0.5° increments, and a Molybdenum target. A maximum resolution of approximately 5 μm was achieved at the highest magnification. The CT Pro software package was used to reconstruct the raw image data while VG Studio Max 1.2 was used for surface rendering to create the three dimensional image of the damaged specimen.

3 Multiscale Failure Model for Fatigue

The failure behavior of the composite subjected to fatigue loading is modeled using the space-time multiscale computational framework previously developed in Ref. [10]. The aim and the main contribution of the current investigation is to employ this computational approach to understand the interaction of the subcritical failure mechanisms that contribute to the composite survivability. A general description of the modeling strategy used is briefly described below, and the constitutive equations of the composite constituents are stated. Detailed multiscaling theory and its implementation are described in Refs. [9, 10, 19] and skipped herein for brevity.

The multiscale computational strategy for fatigue life prediction is illustrated in Fig. 1. In space, the Eigendeformation-based reduced order homogenization (EHM) approach was employed. In this approach, the microstructure response is approximated numerically using a reduced order representation of the characteristic volume (i.e., representative volume element

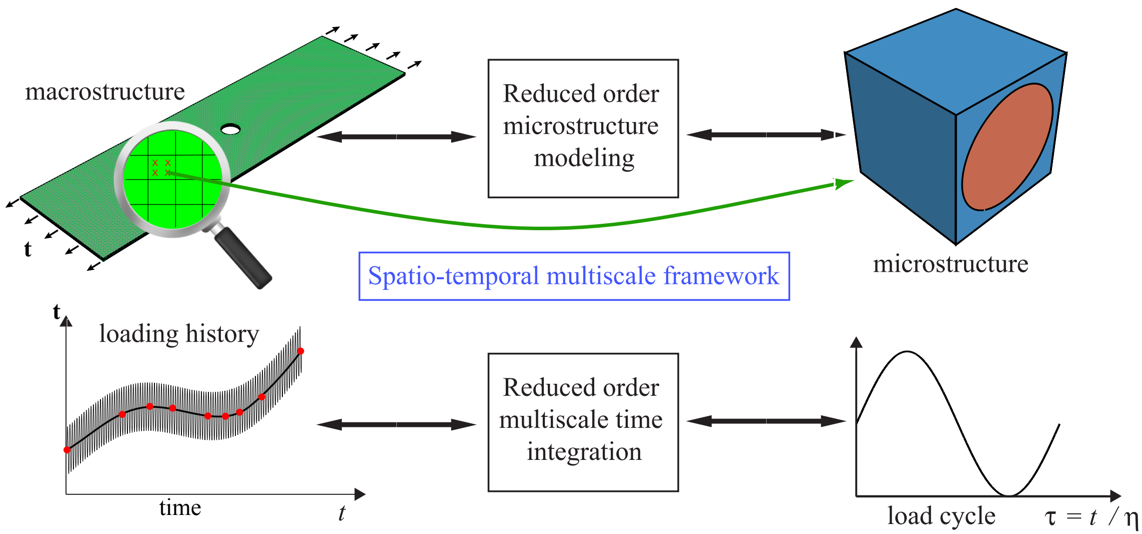

Figure 1: Space-time multiscale computational modeling strategy.

or a unit cell) associated with each quadrature point of the discretized macroscopic domain. EHM is a generalization of the Transformation Field Analysis [11], and employs the idea of precomputing certain information on the material microstructure such as the influence functions, localization operators and coefficient tensors through detailed characteristic volume (CV) simulations prior to the macroscale analysis. The reduced order model is obtained by assuming that the damage and inelastic strain fields are spatially piecewise constant within subdomains of the CV.

Figure 2 illustrates the CV domain partitioning strategy in the context of the unit cell employed in this study. The cubic unit cell consists of two constituents, the graphite fiber reinforcement and the epoxy matrix. The reduced order model associated with the unit cell considers four subdomains (or *failure paths*), within which the damage state is taken to evolve in a piecewise uniform manner. The damage states within the subdomains represent the dominant damage mechanisms in the composite, i.e., fiber fracture, transverse matrix cracking and delamination. We note that the delamination is modeled starting from the scale of the material microstructure, in contrast to cohesive zone modeling (CZM) typically employed to idealize delamination [27]. While CZM has been shown to provide accurate prediction of delamination propagation, it comes with significant computational cost and difficulty in numerical convergence – both of which are alleviated by the current approach. It is also possible to consider other unit cell configurations such as a hexagonal cell or a representative volume with randomly positioned fibers, which exhibit slight differences in the behavior and

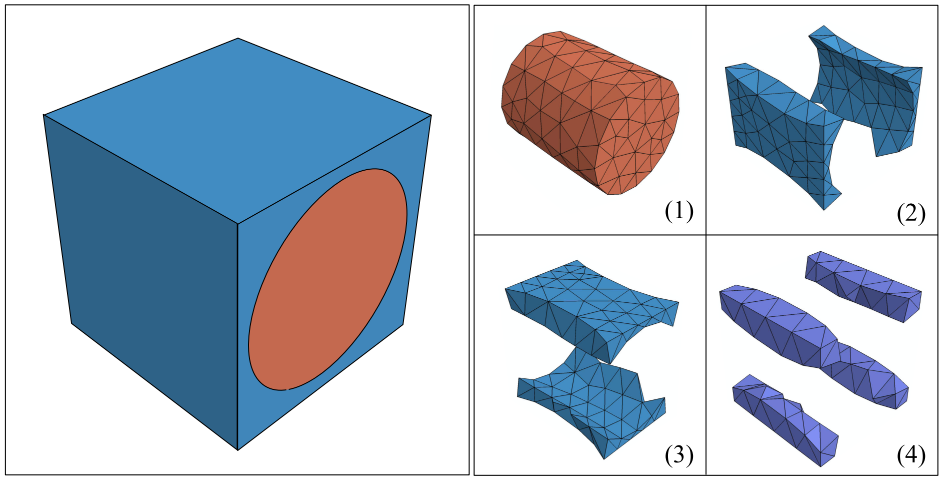

Figure 2: Cubic unit cell for the unidirectional CFRP along with the reduced order partitioning. The failure modes represented by the partitioning are: (1) fiber fracture, (2) transverse matrix cracking, (3) delamination, and (4) delamination-transverse matrix crack interactions.

properties. The resulting failure mechanisms are expected to be similar regardless of the choice of the characteristic volume.

Let $\omega^{(\alpha)} \in [0,1)$ indicate the state of damage associated with the failure path, α, that corresponds to fiber fracture ($\alpha = \mathrm{f}$), transverse matrix cracking ($\alpha = \mathrm{m}$), delamination ($\alpha = \mathrm{d}$) or delamination - transverse matrix cracking interaction ($\alpha = \mathrm{i}$). The evolution of the damage variable is expressed as:

$$\dot{\omega}^{(\alpha)} = \left[\frac{\Phi(\upsilon^{(\alpha)})}{\omega^{(\alpha)}} \right]^{p^{(\alpha)}} \frac{d\Phi(\upsilon^{(\alpha)})}{d\upsilon^{(\alpha)}} \left\langle \dot{\upsilon}^{(\alpha)} \right\rangle_+ \tag{1}$$

where a superscribed dot indicates time derivative, $\langle \cdot \rangle_+$ denotes Macaulay brackets, Φ the phase damage evolution function, $p^{(\alpha)}$ the cycle sensitivity exponent, and $\upsilon^{(\alpha)}$ the damage equivalent strain associated with the failure path, α. The power form in the damage evolution equation ensures that damage accumulates under cyclic loading. The phase damage evolution function is taken to follow an arctangent law of the form:

$$\Phi(\upsilon^{(\alpha)}) = \frac{\mathrm{atan}(a^{(\alpha)} \langle \upsilon^{(\alpha)} - \upsilon_0^{(\alpha)} \rangle - b^{(\alpha)}) + \mathrm{atan}(b^{(\alpha)})}{\frac{\pi}{2} + \mathrm{atan}(b^{(\alpha)})} \tag{2}$$

in which $a^{(\alpha)}$ and $b^{(\alpha)}$ are parameters that control strength and ductility, and $\upsilon_0^{(\alpha)}$ is the threshold damage equivalent strain, below which damage does not evolve. Φ is a non-negative, smooth and monotonically-varying function that asymptotes to unity.

The rate of damage evolution under cyclic loading is controlled by the multiplier component in power form in Eq. 1 (i.e., $(\Phi(\upsilon^{(\alpha)})/\omega^{(\alpha)})^{p^{(\alpha)}}$). The role of this component can be explained by considering an example where the damage equivalent strain is periodically cycled in interval $[0, \upsilon^{(\alpha)}_{\max}]$. In the absence of the multiplier term ($p^{(\alpha)} = 0$), the amount of damage accumulation in each cycle is identical to the first cycle, which constitutes the initial static loading. Damage accumulation is always non-negative due to the monotonic evolution of Φ, and non-zero only during loading (i.e., $\dot{\upsilon}^{(\alpha)} > 0$). In view of the observation that $\Phi(\upsilon^{(\alpha)})/\omega^{(\alpha)} \leq 1$ and by setting $p^{(\alpha)} > 0$, the multiplier term reduces the amount of damage accumulation at subsequent cycles relative to the first cycle. Higher values of the exponent results in slower accumulation of damage under cyclic loading.

$b^{(\alpha)}$ is expressed as a function of the principal and shear strains as:

$$b^{(\alpha)} = k_b^{(\alpha)}\, b_s^{(\alpha)} + (1 - k_b^{(\alpha)})\, b_n^{(\alpha)}; \quad k_b^{(\alpha)} = \frac{2\gamma^{(\alpha)}_{\max}}{\gamma^{(\alpha)}_{\max} + \epsilon^{(\alpha)}_{\max}} \tag{3}$$

where $\gamma^{(\alpha)}_{\max}$ and $\epsilon^{(\alpha)}_{\max}$ are the maximum shear and absolute principal strains within the failure path α, respectively, and $b_s^{(\alpha)}$ and $b_n^{(\alpha)}$ are material parameters controlling the ductility as a function of the strain state. Under pure shear conditions (i.e., $\gamma^{(\alpha)}_{\max} = \epsilon^{(\alpha)}_{\max}$), $k_b^{(\alpha)} = 1$ and the value of $b^{(\alpha)}$ equals $b_s^{(\alpha)}$. Under uniaxial normal loading (i.e., $\gamma^{(\alpha)}_{\max} = \epsilon^{(\alpha)}_{\max}/2$), $k_b^{(\alpha)} = 2/3$ and the ductility parameter becomes: $b^{(\alpha)} = (2b_s^{(\alpha)} + b_n^{(\alpha)})/3$. Under a general state of strain, the value of $k_b^{(\alpha)}$ varies within $[0, 1]$, and vanishes at pure hydrostatic strain state where $b^{(\alpha)}$ equals $b_n^{(\alpha)}$.

Equation 3 has its roots in the critical plane idea [14, 15, 16], and allows to span the brittle failure observed under normal strain to ductile failure under shear strains. The phase damage equivalent strain is defined as a function of the phase average principal strains, $\hat{\boldsymbol{\varepsilon}}^{(\alpha)}$, as:

$$\upsilon^{(\alpha)} = \sqrt{\frac{1}{2}\left(\mathbf{F}^{(\alpha)}\hat{\boldsymbol{\varepsilon}}^{(\alpha)}\right)^T \hat{\mathbf{L}}^{(\alpha)} \left(\mathbf{F}^{(\alpha)}\, \hat{\boldsymbol{\varepsilon}}^{(\alpha)}\right)} \tag{4}$$

where $\hat{\mathbf{L}}^{(\alpha)}$ denotes the tensor of elastic moduli rotated to the principle strain direction, and $\mathbf{F}^{(\alpha)}$ is the weighting matrix that accounts for the tension-compression asymmetry of the failure behavior:

$$\mathbf{F}^{(\alpha)}\left(\mathbf{x},t\right) = \mathrm{diag}\left(h_1^{(\alpha)}, h_2^{(\alpha)}, h_3^{(\alpha)}\right); \quad h_\xi^{(\alpha)}\left(\mathbf{x},t\right) = \begin{cases} 1 \text{ if } \hat{\epsilon}_\xi > 0 \\ c^{(\alpha)} \text{ otherwise} \end{cases} \qquad \zeta = 1,2,3 \tag{5}$$

in which $c^{(\alpha)}$ is a material parameter that represents damage contributions of the tensile and compressive loading in the principle directions, and diag denotes diagonal matrix.

The sensitivity of the damage evolution function to cyclic loading is controlled by the power function, $p^{(\alpha)}$:

$$p^{(\alpha)} = d_0^{(\alpha)} + d_1^{(\alpha)} \upsilon_{\max}^{(\alpha)} + d_2^{(\alpha)} \left(\upsilon_{\max}^{(\alpha)}\right)^2 \tag{6}$$

in which $d_i^{(\alpha)}$ $(i = 1,2,3)$ are material parameters that relate the cyclic damage evolution to the loading history in the respective failure path where $\upsilon_{\max}^{(\alpha)}\left(\mathbf{x},t\right) = \max_{\tau\in[0,t]}\left\{\upsilon^{(\alpha)}\left(\mathbf{x},\tau\right)\right\}$ denotes the maximum value of the phase damage equivalent strain experienced within the failure path, α, throughout the cyclic loading. The quadratic variation of the cycle sensitivity exponent as a function of the peak damage equivalent strain allows a more accurate control of the variation of fatigue life of the constituent with the applied load amplitude. $d_i^{(\alpha)}$ are therefore calibrated using experimental stress-life curves of lamina configurations, where the critical failure mode coincides with the failure mode idealized by part, α.

The macroscale stress (i.e., CV-average) of the composite is expressed as a function of the macroscale strain, $\bar{\boldsymbol{\epsilon}}$, and the phase average damage-induced inelastic strains (i.e., eigenstrains), $\boldsymbol{\mu}^{(\alpha)}$:

$$\bar{\sigma}_{ij}(\mathbf{x},t) = \sum_\alpha \left[1 - \omega^{(\alpha)}(\mathbf{x},t)\right] \left(\bar{L}_{ijkl}^{(\alpha)} \bar{\epsilon}_{kl}\left(\mathbf{x},t\right) + \sum_\gamma \bar{P}_{ijkl}^{(\alpha\gamma)} \mu_{kl}^{(\gamma)}\left(\mathbf{x},t\right)\right) \tag{7}$$

where the damage-induced inelastic strains are computed by solving the following nonlinear equation:

$$\sum_\alpha \left\{\left[1 - \omega^{(\alpha)}\left(\mathbf{x},t\right)\right]\left[C_{ijkl}^{(\eta\alpha)} \bar{\epsilon}_{kl}\left(\mathbf{x},t\right) + \sum_\gamma F_{ijkl}^{(\eta\alpha\gamma)} \mu_{kl}^{(\gamma)}\left(\mathbf{x},t\right)\right]\right\} = 0; \quad \eta = \mathrm{f},\mathrm{m},\mathrm{d},\mathrm{i} \tag{8}$$

in which the coefficient tensors $\bar{\mathbf{L}}^{(\alpha)}$, $\bar{\mathbf{P}}^{(\alpha\gamma)}$, $\bar{\mathbf{C}}^{(\eta\alpha)}$ and $\bar{\mathbf{F}}^{(\eta\alpha\gamma)}$ are functions of a series of influence functions (i.e., numerical approximations to Green's function problems) defined over the CV. The coefficient tensors are computed a-priori and effectively serve as constitutive tensors that contain the microstructural morphology information.

Prediction of the progressive damage accumulation under the high cycle fatigue regime is performed by employing a multiple time scale life prediction model [9]. The multiple time scale analysis is based on the generalization of homogenization principles to the time domain. In this approach, time scale asymptotic analysis is performed on the equations that govern equilibrium and damage evolution, which results in a coupled system of micro-chronological (i.e., fast time scale) and macro-chronological (i.e., slow time scale) problems (Fig. 1). The micro-chronological problem evaluates the response of the composite specimen subjected to a single load cycle, whereas the macro-chronological problem provides the long-term evolution of damage and equilibrium state within the specimen. The numerical evaluation of this coupled, multichronological system resembles the characteristics of the block-cycle modeling [21], where the damage accumulation rate is computed through a few load cycle analyses throughout the fatigue life. The multiple time scale approach employed in this manuscript is advantageous as it maintains equilibrium and thermodynamic consistency throughout the loading process [9].

4 Model Preparation

4.1 Model Calibration

The parameters of the multiscale model were calibrated based on the calibration experiments as summarized in Table 1. The calibration of the model parameters was performed in two stages, separately, for the static and fatigue parameters. The three dominant failure modes are represented by the three failure paths (Fig. 2) and modeled using separate failure parameters. The static failure parameters of a given failure path, α, are $a^{(\alpha)}$, $b_s^{(\alpha)}$, $b_n^{(\alpha)}$, $\nu_0^{(\alpha)}$ and $c^{(\alpha)}$. The interaction path parameters are taken to be identical to the matrix-cracking mode. The model therefore requires the identification of 15 parameters to describe failure under static loading. While it is possible to identify all parameters simultaneously through a parameter identification process [20], this typically is too costly due to high dimensionality of the parameter space. The parameters were separated into sets and identified against experiments that exhibit highest sensitivity.

The uniaxial tension tests on unidirectional laminates were used to calibrate the fiber failure parameters (i.e., $a^{(\mathrm{f})}$, $b_n^{(\mathrm{f})}$, $\nu_0^{(\mathrm{f})}$). The zero degree uniaxial compression test was employed to calibrate the tension-compression anisotropy parameter, $c^{(\mathrm{f})}$. $b_s^{(\mathrm{f})}$ is taken as unity since the fiber is expected to fail in a brittle manner. The parameters that model matrix cracking were identified based on the three-point bend experiments to obtain $a^{(\mathrm{m})}$, $b_n^{(\mathrm{m})}$ and $\nu_0^{(\mathrm{m})}$, ninety degree uniaxial compression to obtain $c^{(\mathrm{m})}$, and $[+45, -45]_{2S}$ and V-notch shear tests to obtain $b_s^{(\mathrm{m})}$. The end notch flexure testing was employed to calibrate $a^{(\mathrm{d})}$, $b_n^{(\mathrm{d})}$, $b_s^{(\mathrm{d})}$ and $\nu_0^{(\mathrm{d})}$, whereas the compression-tension anisotropy parameter was taken to be identical to the matrix cracking mode. Calibrations that involved multiple parameters were performed using sequential quadratic programming, where the optimal parameter set is identified by obtaining the best least squares fit between the experimental and simulated stress-strain curves. The overview of the lamina level fit between the experiments and simulations is provided in Table 2.

Table 2: Monotonic calibration results.

Parameter	Description	Experiment average	Simulated value
E_{zt} (GPa)	Longitudinal tension modulus	164.3	163.9
E_{zc} (GPa)	Longitudinal compression modulus	137.4	137.4
E_x (GPa)	Transverse modulus	8.85	8.85
G_{zy} (GPa)	Shear modulus	4.94	4.94
ν_{zx}	Longitudinal Poisson's ratio	0.3197	0.321
ν_{xz}	Transverse Poisson's ratio	0.0175	0.0173
X_T (MPa)	Longitudinal tension strength	2,905	2,905
X_C (MPa)	Longitudinal compression strength	1,680	1,680
Y_T (MPa)	Transverse tension strength	130	130
Y_C (MPa)	Transverse compression strength	247.6	247.7

The fatigue failure parameters for each of the three failure modes consist of $d_0^{(\alpha)}$, $d_1^{(\alpha)}$ and $d_2^{(\alpha)}$, leading to a total of nine fatigue sensitive parameters. Similar to the monotonic calibrations, these parameters were calibrated based on stress-life curves of zero degree uniaxial, ninety degree three-point bend and end notch flexure fatigue testing for fiber fracture, matrix cracking and delamination modes, respectively. The calibrated parameters are provided in Table 3.

4.2 Specimen Discretization

The geometry and the discretization of the open-hole $[60,0,\text{-}60]_{3S}$ specimens are shown in Fig. 3. The specimen is discretized using 79,551 hexahedral or wedge elements and 131,064 nodes. The size of the elements is approximately 1 mm in the in-plane directions. In order to avoid mesh sensitivity, all meshes in the calibration and prediction simulations employ

Table 3: Calibrated model parameters.

Property	Fiber	Matrix	Delamination
a	0.050562	0.001592	0.018
b_n	274	15	304 .0
b_s	-	-3.2	9.45
c	1.4481	0.535	0.492
υ_0	1367	636.2	0
d_0	10.735	6.0	6.0
d_1	-2.068×10^{-3}	-3.0×10^{-3}	-6.0×10^{-3}
d_2	-1.04×10^{-10}	-2.62×10^{-10}	-2.62×10^{-10}

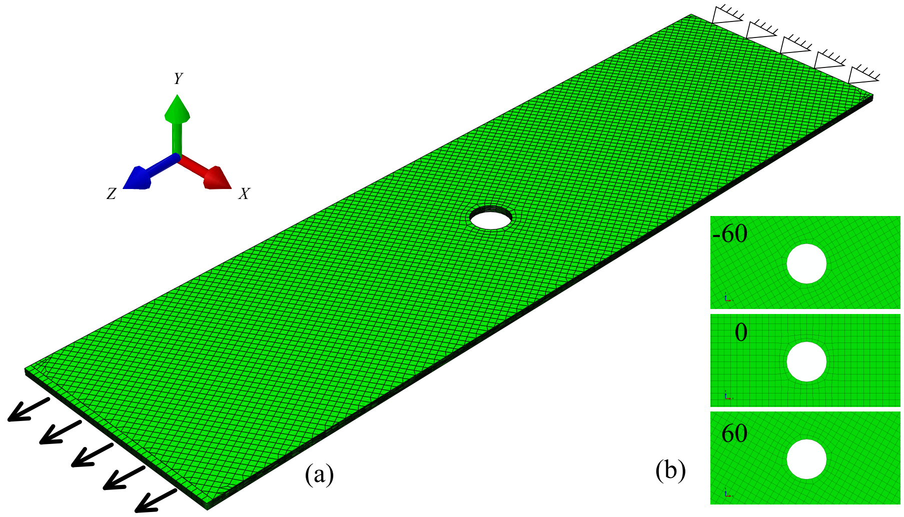

Figure 3: Numerical specimen with $[60,0,\text{-}60]_{3S}$ layup: (a) geometry, boundary and loading conditions; and (b) mesh orientation of the lies near the hole.

elements of the same size. In order to avoid mesh bias, the discretization within each ply follows the fiber orientation. Every ply in the laminate is modeled, and the plies are connected using multipoint constraints due to mesh incompatibility between the plies. All off-axis plies have a single element discretizing the thickness direction, whereas zero degree plies have three elements along the thickness direction to better capture post-delamination kinematics. The computations of the stress, strain and compliance are made consistent with the experimental observations.

5 Results of the Experimental-Computational Study

Figure 4 illustrates the state of damage within a representative $[60,0,\text{-}60]_{3S}$ specimen tested in the study, through 200K loading cycles as observed using X-ray radiography. The other

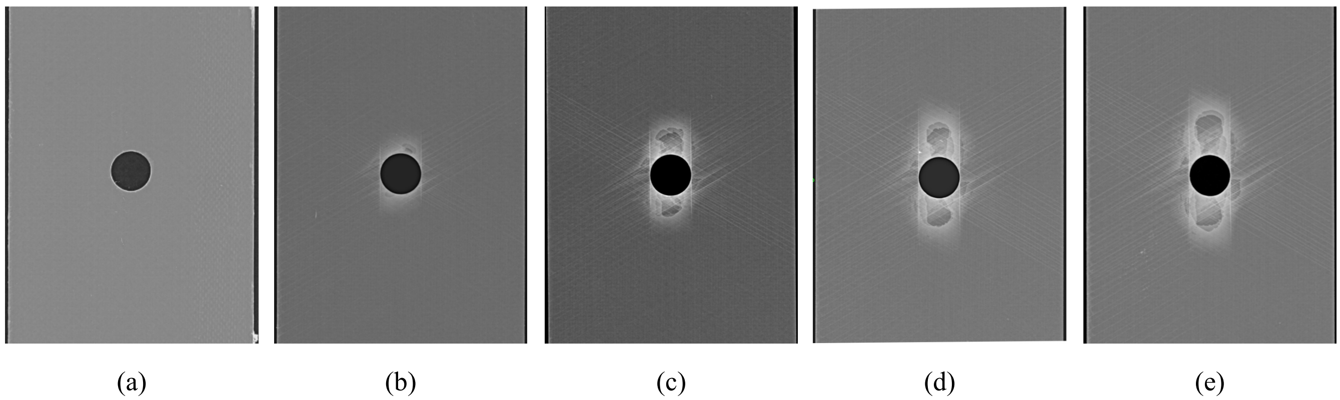

Figure 4: X-ray radiography images of the $[60,0,\text{-}60]_{3S}$ specimen: (a) initial state, after (b) 50K, (c) 100K, (d) 150K, and (e) 200K cycles.

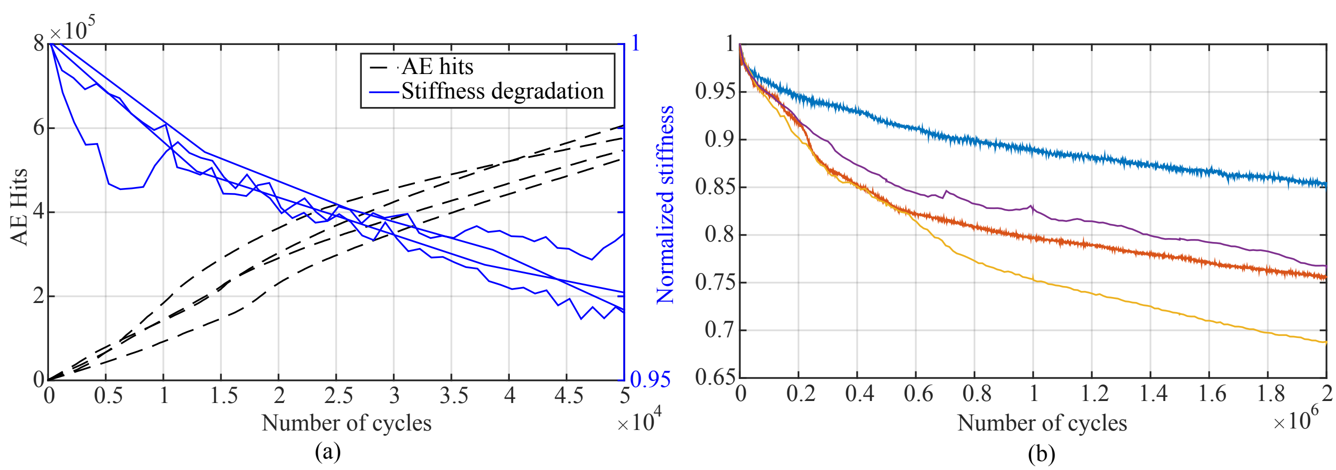

Figure 5: Acoustic Emission hits and stiffness degradation as a function of load cycles for four identical $[60,0,\text{-}60]_{3S}$ specimens.

specimens exhibited similar damage patterns. The images show damage at all plies through the thickness of the specimen. The loading is applied along the north-south direction. The initial state of the specimen is largely defect free with possibly very slight delamination around the hole (Fig. 4a). The damage region around the hole progressively increases as a function of load cycles with snapshots shown for every 50K cycles. The rate of progressive damage accumulation is very stable within this range of cycles. Figure 5a further supports the assertion that the nature of damage accumulation is progressive throughout stiffness reduction and acoustic emission hits as a function of load cycles, shown up to 50K cycles. The damage growth as correlated to the reduction of the secant modulus of the coupon and the number of AE hits gradually increases with no indication of a change in the damage mode, which would otherwise register a discontinuity or abrupt rate change in the curves. We note that Fig. 5a does not distinguish between propagation of different damage mechanisms that contribute to the property degradation.

Figure 6 shows the damage modes within the $[60,0,\text{-}60]_{3S}$ specimen that grow under fatigue loading. The close-up image is obtained by 3-D X-ray computed tomography, where the focus in each image moves through the thickness of the laminate for each ply. Starting from the image in the top left for the 60 ply at the surface, the images continue left to right and top to bottom moving towards the midplane of the specimen. In these images, distinct white lines indicate matrix cracking and larger white regions indicate zones of delamination. We note that damage in the plies behind the interface bleeds over to the image. The figure clearly shows matrix cracking at the ± 60 plies and fiber splitting at the 0 plies. From the micro-mechanism perspective, fiber splitting and matrix cracking are identical and fiber splitting refers to matrix cracking in the 0 plies. At the 60-0 interface, a large delamination zone exists at the top and bottom of the hole, delimited by the extent of fiber splitting. While the progressive damage accumulation continues throughout the loading history, none of the $[60,0,\text{-}60]_{3S}$ specimens failed within the two million cycle observation period. Figure 5b shows the degradation of the composite stiffness in four separate $[60,0,\text{-}60]_{3S}$ open-hole specimens, with the same configuration as the specimen shown in Figure 4, up to two million cycles. The general trend points to a slowdown of damage accumulation past approximately 500K cycles. The fact that none of the specimens failed implies that all damage modes remain subcritical, despite the large amplitude of the applied cyclic load (80% of the monotonic strength).

In order to understand the role of interacting subcritical damage mechanisms on the fail-

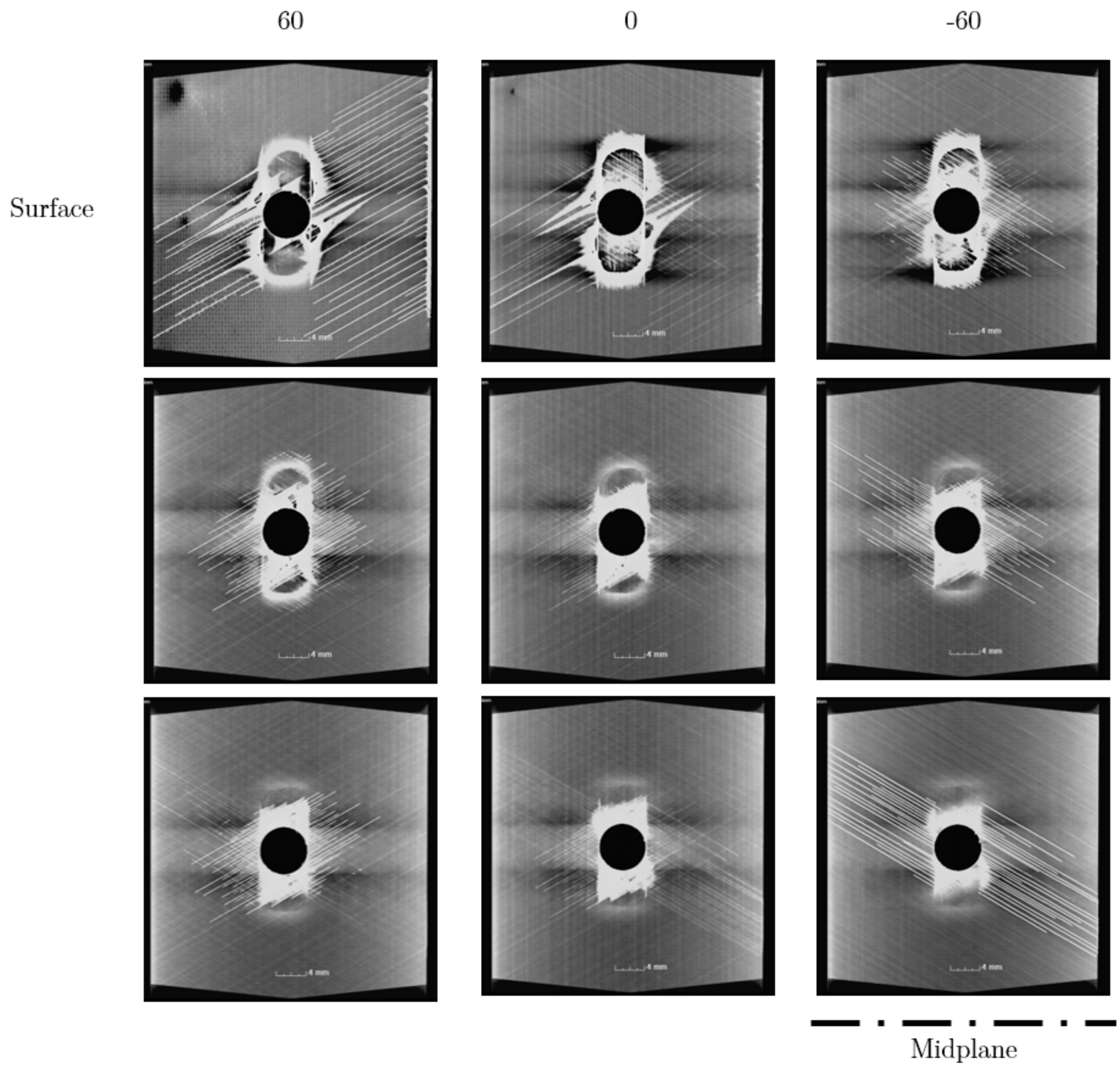

Figure 6: X-ray computed tomography images of the $[60,0,-60]_{3S}$ specimen after 150K cycles illustrating the damage modes.

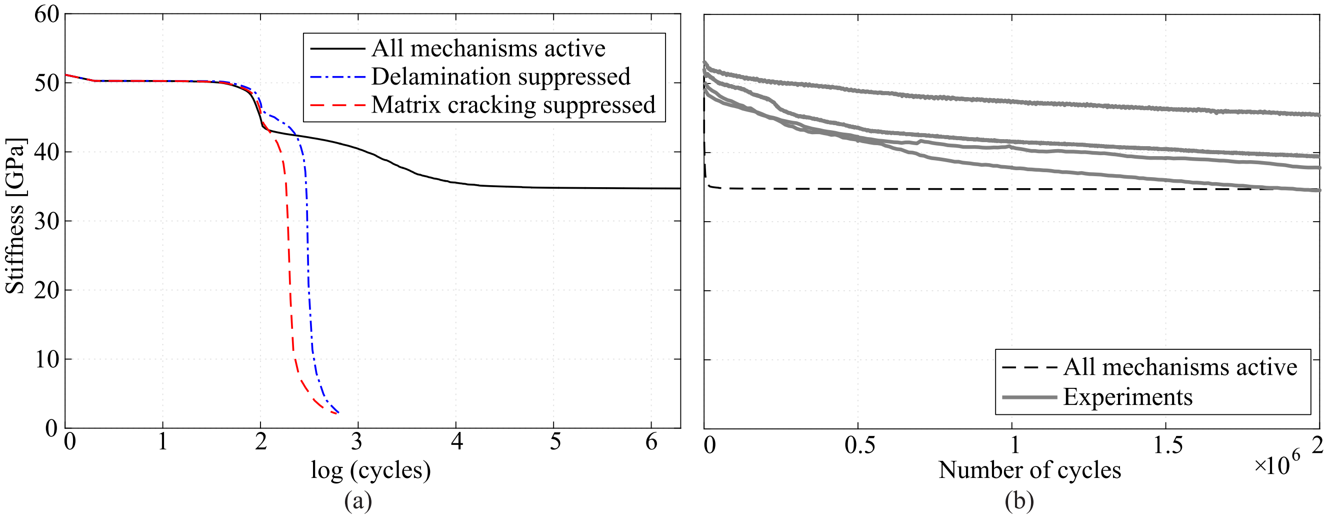

Figure 7: Stiffness degradation of $[60,0,\text{-}60]_{3S}$ numerical simulations.

ure behavior under fatigue loading, numerical simulations were performed using the calibrated multiscale model. In the first simulation, the model includes fiber failure and matrix cracking as possible damage mechanisms. The possibility of delamination is deliberately excluded to understand its role on the failure response and overall fatigue life. In Figures 8-10, two representative plies nearest the mid-plane of the laminate are shown which demonstrate the damage progression modes present in the laminate. Surface effects notwithstanding, similar damage behavior was observed over all plies of the same orientation in the laminate.

Figures 7a and 8 show the stiffness loss and the representative damage contours from the numerical simulation. In the absence of delamination, the stiffness of the composite specimen degrades very quickly, within approximately 300 cycles causing failure of the specimen. The damage contours (Fig. 8) show a quick progressive matrix cracking in the 60 plies. The matrix cracking is accompanied by fracture of the fibers within the zero degree plies that initiate around the hole and propagate outward towards the specimen edges and ultimately cause the specimen failure. In contrast with the numerical simulation results, the experiments did not exhibit such a substantial fiber cracking. Fiber splitting, which is prevalent in all experimental specimens also did not form in the numerical simulation. The discrepancy between the failure modes observed in the simulation and the experiments point to the role of delamination in determining the failure characteristics of the composite subjected to fatigue loading.

The stiffness degradation of a numerical simulation that includes delamination as a possible failure mechanism but suppresses the growth of matrix cracking in just the 0 plies is shown

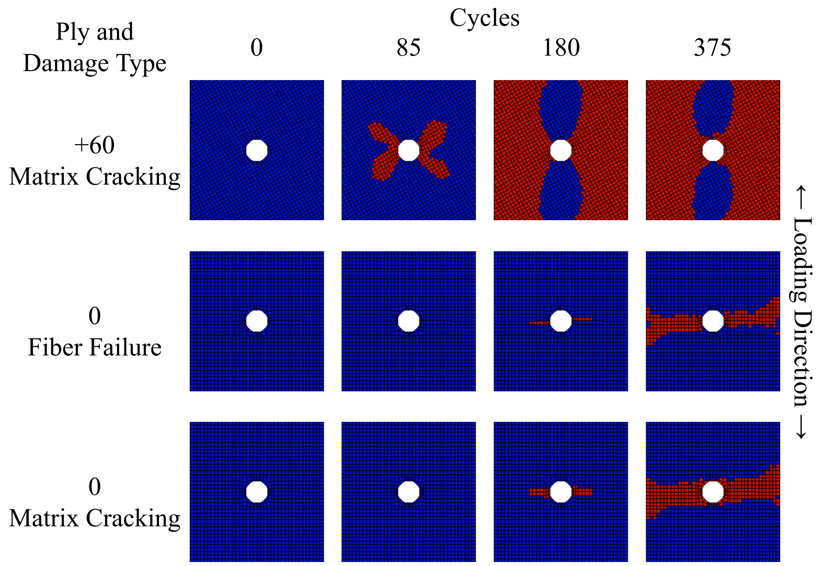

Figure 8: Damage contours of the $[60,0,\text{-}60]_{3S}$ numerical simulation with delamination failure suppressed.

in Figure 7a. This simulation case also exhibited premature global failure as compared to the experiments. Similar to the previous simulation with delamination suppressed, the simulation exhibited transverse matrix cracking failure in the off-axis plies within the initial loading cycles. Figure 9 shows this damage mechanism, as well as the additional failure mechanisms leading up to the global failure of the specimen. At the early stage of the loading process, the initiation of fiber failure around the hole in the 0 plies is observed, and this damage mechanism propagates within 200 cycles towards the edges of the coupon, leading to specimen failure. The propagation of fiber failure transverse to the loading direction throughout the loading was not observed in the 0 plies in the experiments. From these two numerical investigations, it is clear that delamination failure alone or transverse matrix failure alone are not sufficient to describe the failure of the $[60,0,\text{-}60]_{3S}$ specimen.

Figure 7a includes the stiffness evolution predicted by the calibrated multiscale model, whereas Fig. 7b shows the comparison of the stiffness evolution predictions along with the experimental data. In contrast to the previous two cases, in which one of the two subcritical damage modes are suppressed, the current simulation does not predict a premature fatigue failure. At the early stage of loading, a significant amount of damage occurs, manifested by a drop in the stiffness of the specimen. The damage accumulation rate reduces significantly thereafter, and the specimens run out beyond two millions cycles. The damage modes and

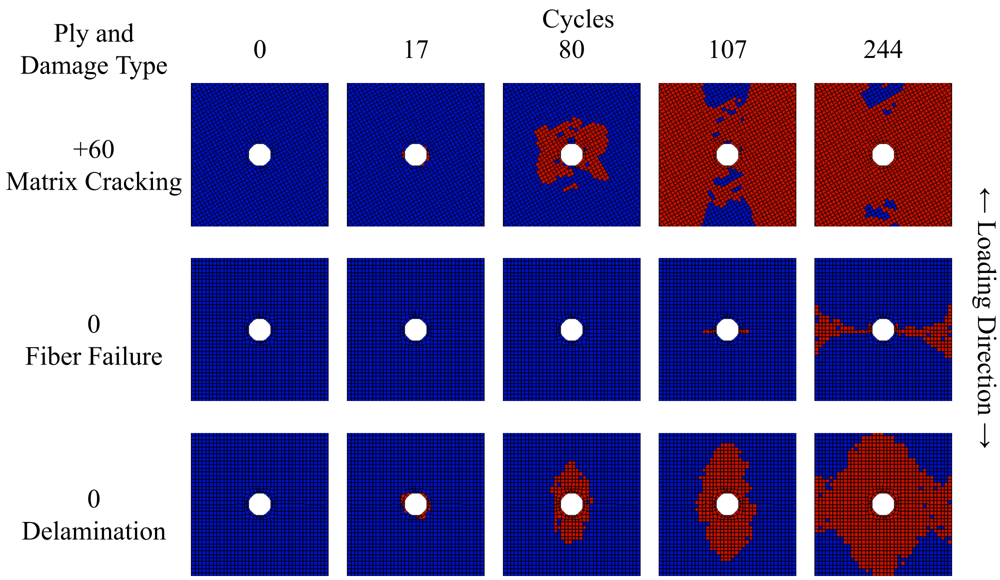

Figure 9: Damage contours of the $[60,0,-60]_{3S}$ numerical simulation with matrix cracking failure suppressed in the 0 plies.

the accumulation characteristics predicted by the model are very similar to those observed experimentally, as shown in Fig. 11 which shows a comparison between CT images of the interior plies $[60,0,-60]_{3S}$ laminate after 150k fatigue cycles compared with corresponding images showing damage growth in the simulation. It is noted that the simulation model reaches this damage state more rapidly than observed in experiments, but the qualitative behavior and damage propagation mechanisms are consistent. Fiber splitting and delamination growth are the two dominant damage mechanisms, whereas fiber fracture propagation is not observed. We note that the amplitude of loading applied is sufficient to lead to fiber fracture around the hole. While the early onset of fiber fracture is observed in this simulation, the fiber fracture does not propagate transverse to the loading direction. Despite the discrepancy between the experimentally observed and predicted stiffness loss curves, the damage modes and the propagation characteristics are accurately represented when both dominant subcritical modes are included in the model. When either one is absent from the model, the simulations exhibit a drastically different failure pattern compared to the experiments.

The discrepancy between the experimental and simulation results is mostly due to the faster rate of predicted fatigue damage accumulation in the model predictions. This is attributed to two factors, which will be investigated in the near future. First, the fatigue delamination model is calibrated using the end notch flexure specimens, which appear to be insufficient to

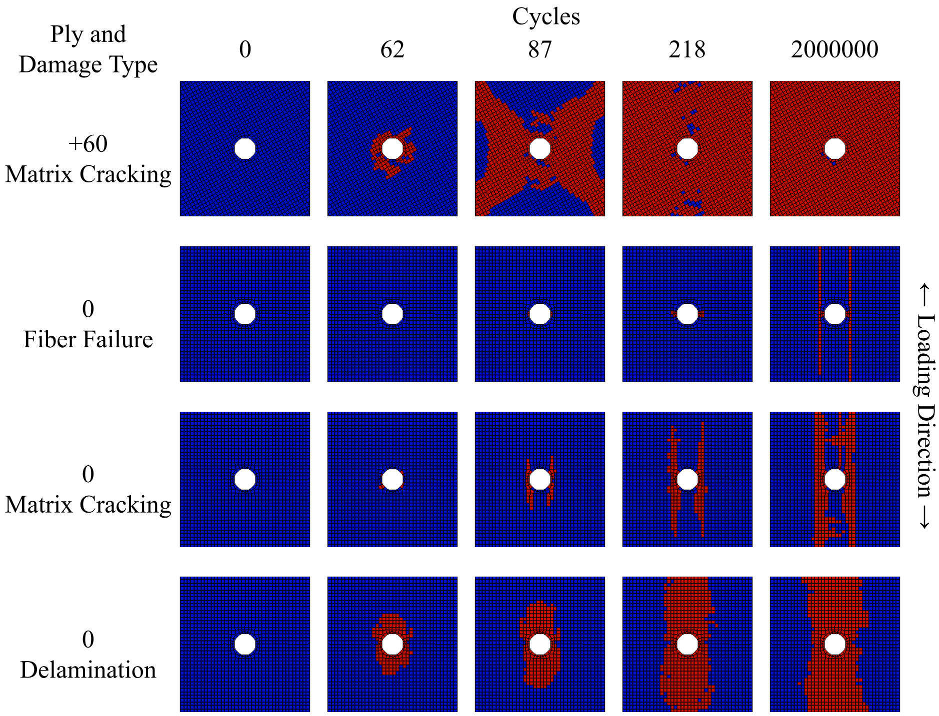

Figure 10: Damage contours of the $[60,0,\text{-}60]_{3S}$ numerical simulation with matrix cracking and delamination present.

properly describe the interlaminar shear dominated damage evolution observed in the open hole specimens. Additional calibration experiments are needed to more accurately describe delamination propagation under fatigue. Second is the apparent difference in the characteristic length describing the fracture process zone (FPZ) between the monotonic and fatigue loading. Fatigue loading leads to a more widespread damage around the notch compared to the monotonic loading as evidenced by X-ray images. The strength parameters are calibrated based on monotonic loading, but also affect the fatigue properties in the current numerical model. A careful quantification of the nonlocal effects in the material may lead to a better quantitative match between the experiments and the simulations. We further note that no attempt was made to better match the experimental data beyond proper calibration with the calibration experiments.

6 Discussion of Failure Interactions

The combined experimental-computational investigation described above indicates a strong interactive effect of subcritical damage mechanisms on the fatigue survivability of laminated

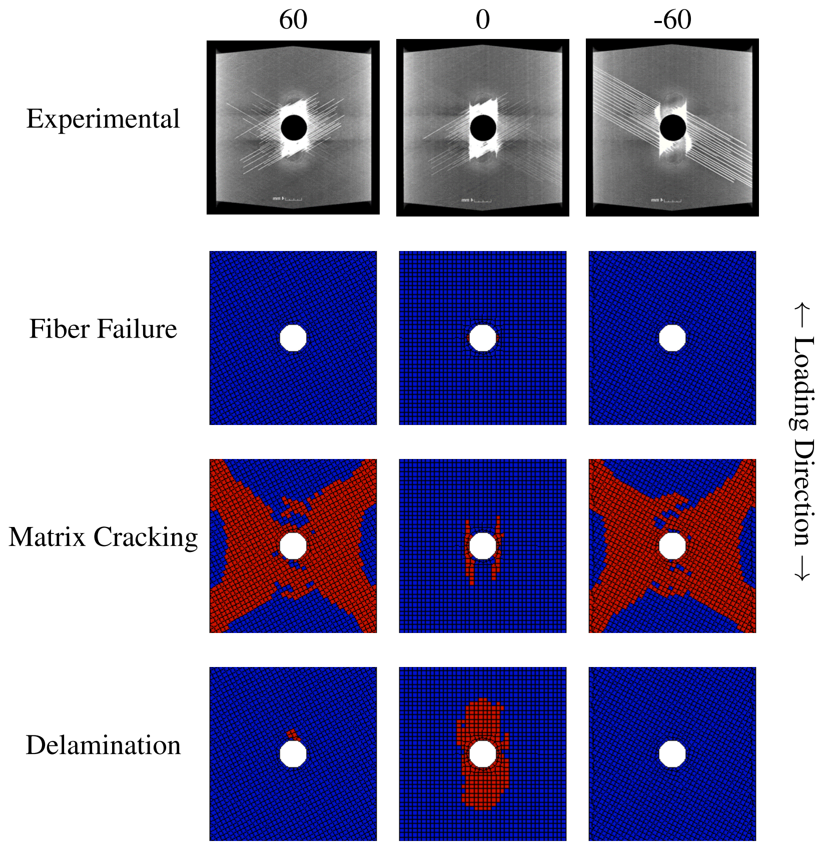

Figure 11: Damage contours of the $[60,0,-60]_{3S}$ numerical simulation with matrix cracking and delamination present compared with images from experimental CT images.

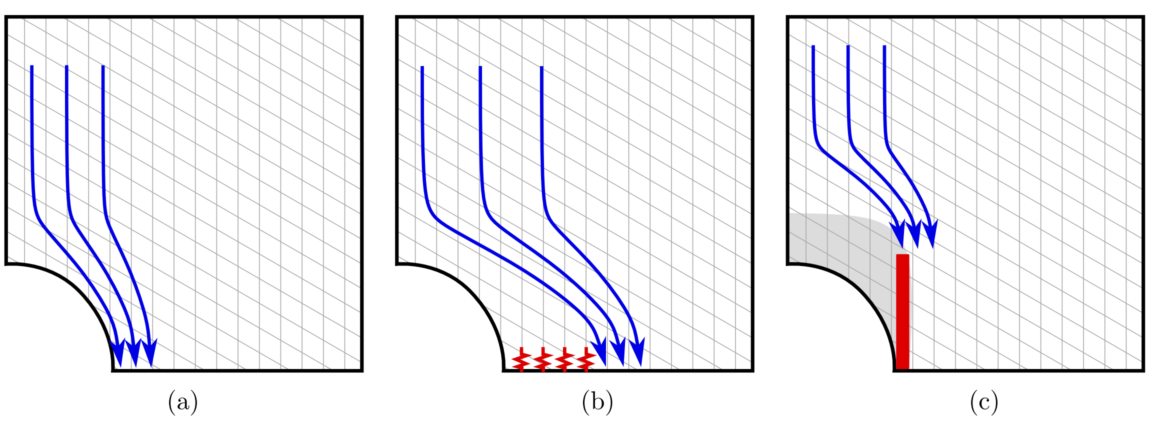

Figure 12: Schematic illustration of the stress concentration path and interaction of damage mechanisms in the 0/60 plies of the $[60,0,-60]_{3S}$ specimen: (a) Stress concentration at initial loading; (b) fiber fracture propagation in the absence of delamination; and (c) fiber splitting and delamination near the notch when all damage modes are active.

composites under high amplitude fatigue loading. This investigation indicates that the following cascade of damage events controls the failure in the specimen as illustrated by Fig. 12 dictated by the presence or absence of delamination around the zero-degree plies. Under the applied cyclic loading, a stress concentration is present around the open hole, which for high amplitude stresses can lead to fiber failure at the edges of the open hole. This stress concentration is illustrated in Fig. 12a. In the experimental specimens, an interlaminar shear dominated delamination occurs around the notch between the zero-degree and the off-axis plies that induces fiber splitting in the matrix of the zero-degree plies, Fig. 12c. Fiber splits cause the relaxation of the stress concentration around the hole and redistribute the loading more evenly along the zero-degree plies, reducing the stress on the fibers near the hole. The reduction of the stresses on the fibers arrests the propagation of the fiber fracture transverse to the loading direction.

In the absence of delamination this phenomenon cannot occur. Shear stresses that cause fiber splitting are bridged by the neighboring off-axis plies around the hole. The stress concentration is not relieved and the fiber fracture propagates as a crack through the specimen. This process is schematically illustrated in Fig. 12b.

We note that this phenomenon is not specific to the laminate considered in this study. Spearing and Beaumont [24] also observed the phenomenon of fiber splitting induced relaxation mechanism in quasi-isotropic samples. In their case, the zero-degree surface plies quickly formed fiber splits under fatigue loading. When the zero degree plies are on the surface, the delamination mechanism is no longer needed, as the plies are already kinematically unrestricted from splitting.

Further evidence of the stress relaxation effect is observed in the form of residual strength after fatigue of laminated composite specimens, i.e. the ultimate strength of the specimen in monotonic tension after that specimen has undergone a prescribed number of fatigue loading cycles. Figure 13 shows the residual strength after fatigue of quasi-isotropic ($[+45,0,-45,90]_{2S}$) specimens as a function of the applied fatigue load amplitude. The mean monotonic ultimate strength of the pristine samples of this configuration was measured to be 475 MPa. The residual strengths were measured after subjecting each specimen to 200K constant amplitude tension fatigue cycles with an R-ratio of 0.1. Interestingly, one observes an increase in the strength from the virgin strength when specimens are subjected to fatigue cycles. The corresponding damage profiles induced by prior fatigue loading is shown in Fig. 14. This figure further

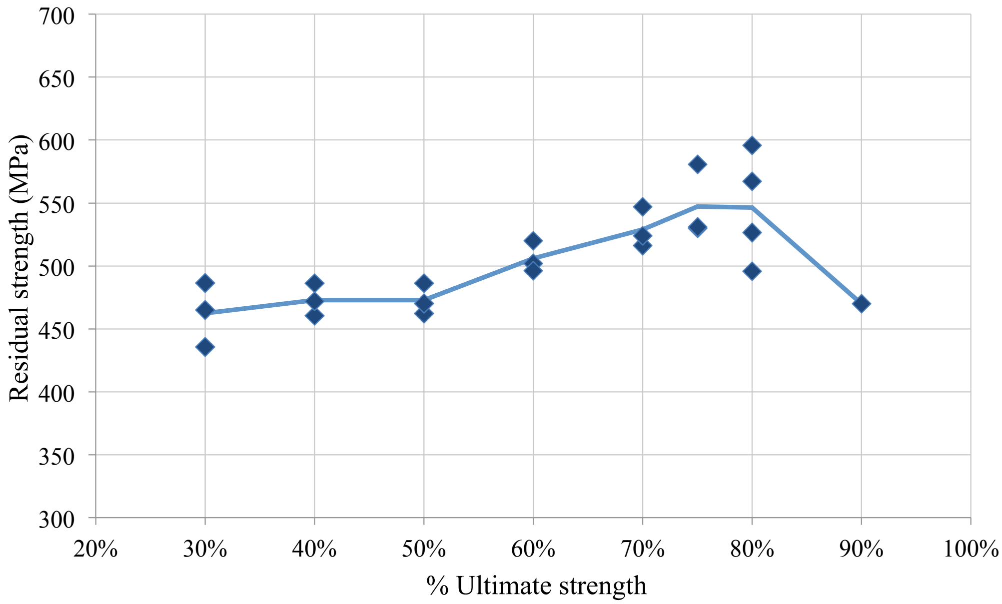

Figure 13: Residual strength after 200K fatigue cycles of $[+45,0,-45,90]_{2S}$ specimens as a function of fatigue load amplitude.

demonstrates that the subcritical damage mechanism of delamination induced fiber splitting relieves the stress concentration and results in a consequent increase of residual strength. While this phenomenon has been previously observed, the connection of its occurrence to the interacting damage modes was not made.

The role of interacting damage mechanisms and their accumulation on the fatigue survivability of laminated composites is particularly important at high amplitude fatigue loading, where significant early fiber fracture is likely to occur. At lower amplitude loading, the fibers are able to carry the loads without the need to redistribute the load. The subcritical damage mechanisms therefore may not have as large an impact on specimen survivability.

7 Conclusions

This manuscript provided a combined experimental - computational investigation of the interactions between the evolving damage mechanisms in CFRPs under high cycle fatigue. A carefully calibrated space-time multiscale computational model has been employed to investigate the behavior in a $[60,0,-60]_{3S}$ sample. The following key conclusions are drawn: (1) The ultimate fatigue life as well as the residual strength and stiffness properties of the composite are directly influenced by the interactions between all failure mechanisms; and (2) suppression

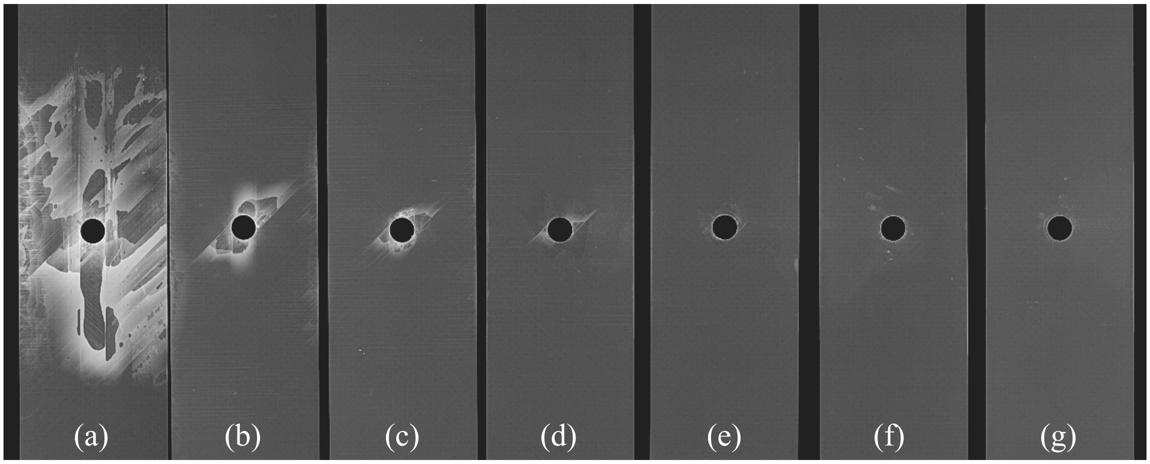

Figure 14: X-ray radiography images of the $[+45,0,-45,90]_{2S}$ specimens subjected to 200K cycles of loading with maximum amplitude of (a) 90%; (b) 80%; (c) 70%; (d) 60%; (e) 50%; (f) 40%; and (g) 30% of mean monotonic ultimate strength.

of a failure mechanism (e.g., delamination through interface design such as z-pinning, etc.), while possibly increasing some of the static properties, could cause a reduction of the long term properties of the composite.

8 Acknowledgement

The authors gratefully acknowledge the financial support provided by the Air Force Research Laboratory (Contract No: GS04T09DBC0017) and Office of Naval Research (Grant No: N00014-17-1-2040; P.O.: William C. Nickerson).

References

[1] A. Afaghi-Katibi, L. Ye, and Y. W. Mai. An experimental study of the infuence of fibre-matrix interface on fatigue tensile strength of notched composite laminates. *Compos. Part B: Eng.*, 32:371–377, 2001.

[2] R. Ambu, F. Aymerich, and F. Bertolino. Investigation of the effect of damage on the strength of notched composite laminates by digital image correlation. *J. Strain Analysis*, 40:451–461, 2005.

[3] F. Aymerich and M. S. Found. Response of notched carbon/PEEK and carbon/epoxy

laminates subjected to tension fatigue loading. *Fatigue Fract. Engng. Mater. Struct.*, 23: 675–683, 2000.

[4] A. Benssousan, J. L. Lions, and G. Papanicolaou. *Asymptotic Analysis for Periodic Structures*. North-Holland, Amsterdam, 1978.

[5] M. J. Bogdanor and C. Oskay. Prediction of progressive damage and strength of im7/977-3 composites using the eigendeformation-based homogenization approach: Static loading. *J. Composite Mater.*, 51:1455–1472, 2017.

[6] M. J. Bogdanor and C. Oskay. Prediction of progressive fatigue damage and failure behavior of im7/977-3 composites using the reduced-order multiple space-time homogenization approach. *J. Composite Mater.*, 51:2101–2117, 2017.

[7] V. L. Chen, H. Y. T. Wu, and H. Y. Yeh. A parametric study of residual strength and stiffness for impact damaged composites. *Compos. Struct.*, 25:267–275, 1993.

[8] R. D. Crouch and C. Oskay. Symmetric meso-mechanical model for failure analysis of heterogeneous materials. *Int. J. Mult. Comp. Eng.*, 8:447–461, 2010.

[9] R. D. Crouch and C. Oskay. Accelerated time integrator for multiple time scale homogenization. *Int. J. Numer. Meth. Engng.*, 101:1019–1042, 2015.

[10] R. D. Crouch, C. Oskay, and S. B. Clay. Multiple spatio-temporal scale modeling of composites subjected to cyclic loading. *Comp. Mech.*, 51:93–107, 2013.

[11] G. J. Dvorak. Transformation field analysis of inelastic composite materials. *Proc. R. Soc. Lond. A*, 437:311–327, 1992.

[12] E. K. Gamstedt and S. Ostlund. Fatigue propagation of fibre-bridged cracks in unidirectional polymer-matrix composites. *Appl. Comp. Mater.*, 8:385–410, 2001.

[13] E. K. Gamstedt and R. Talreja. Fatigue damage mechanisms in unidirectional carbon-fibre-reinforced plastics. *J. Mater. Sci.*, 34:2535–2546, 1999.

[14] A. Gilat, R. K. Goldberg, and G. D. Roberts. Strain rate sensitivity of epoxy resin in tensile and shear loading. *J. Aero. Eng.*, 20:75–89, 2007.

[15] T. Lagoda, E. Macha, and W. Bedkowski. A critical plane approach based on energy concepts: application to biaxial random tension-compression high-cycle fatigue regime. *International Journal of Fatigue*, 21:431–443, 1999.

[16] L. Malcher and E. N. Mamiya. An improved damage evolution law based on continuum damage mechanics and its dependence on both stress triaxiality and the third invariant. *Int. J. Plasticity*, 56:232 – 261, 2014.

[17] J. A. Mohandesi and B. Majidi. Fatigue damage accumulation in carbon/epoxy laminated composites. *Mater. Design*, 30:1950–1956, 2009.

[18] O. J. Nixon-Pearson, S. R. Hallett, P. J. Withers, and J. Rouse. Damage development in open-hole composite specimens in fatigue. part 1: Experimental investigation. *Compos. Struct.*, 106:882–889, 2013.

[19] C. Oskay and J. Fish. Eigendeformation-based reduced order homogenization for failure analysis of heterogeneous materials. *Comput. Methods Appl. Mech. Engrg.*, 196:1216–1243, 2007.

[20] C. Oskay and J. Fish. On calibration and validation of eigendeformation-based multiscale models for failure analysis of heterogeneous systems. *Comp. Mech.*, 42:181:195, 2008.

[21] M. H. J. W. Paas, P. J. G. Schreurs, and W. A. M. Brekelmans. A continuum approach to brittle and fatigue damage: Theory and numerical procedures. *Int. J. Solids. Struct.*, 30:579–599, 1993.

[22] K. L. Reifsnider and A. Talug. Analysis of fatigue damage in composite laminates. *Int. J. Fatigue*, 2:3–10, 1980.

[23] P. A. Sparks and C. Oskay. The method of failure paths for reduced-order computational homogenization. *Int. J. Mult. Comp. Eng.*, 14:515–534, 2016.

[24] S. M. Spearing and P. W. R. Beaumont. Fatigue damage mechanics of composite materials I: Experimental measurement of damage and post-fatigue properties. *Compos. Sci. Technol.*, 44(159-168), 1992.

[25] S. M. Spearing, P. W. R. Beaumont, and M. F. Ashby. Fatigue damage mechanics of composite-materials 2. A damage growth-model. *Compos. Sci. Technol.*, 44:169–177, 1992.

[26] P. M. Suquet. Elements of homogenization for inelastic solid mechanics. In E. Sanchez-Palencia and A. Zaoui, editors, *Homogenization Techniques for Composite Media*. Springer-Verlag, 1987.

[27] H. Yan, C. Oskay, A. Krishnan, and L. R. Xu. Compression after impact response of woven fiber reinforced composites. *Compos. Sci. Technol.*, 70:2128–2136, 2010.